

Real-time exciton dynamics in two-dimensional materials under ultrashort laser pulses

Dmitry Tumakov^{1,2,*} and Daria Popova-Gorelova^{3,2,†}

¹*Department of Physics and CSMB, Humboldt-Universität zu Berlin,
Zum Großen Windkanal 2, Berlin 12489, Germany*

²*I. Institute for Theoretical Physics, University of Hamburg, Notkestraße 9-11, Hamburg 22607, Germany*

³*Institute of Physics, Brandenburg University of Technology Cottbus-Senftenberg,
Erich-Weinert-Straße 1, Cottbus 03046, Germany*

The optical response of two-dimensional materials is often significantly impacted by excitonic effects due to the reduced screening of attractive Coulomb interactions in low-dimensional systems. Accurate modeling of exciton formation and real-time dynamics is essential to understanding their ultrafast optical properties. In this study, we theoretically investigate the exciton dynamics in a two-dimensional hexagonal boron nitride (h-BN) and a germanium sulfide (GeS) monolayers exposed to an ultrashort laser pulse. We analyze the system's response to the external field in one- and two-photon excitation regimes. For our calculations, we combine a state-of-the-art ab initio approach to study exciton dynamics with a highly precise numerical scheme. We incorporate electron-hole interactions through a non-local self-energy operator derived from the many-body perturbation theory (MBPT) within the time-dependent adiabatic *GW* (TD-a*GW*) approximation. We implement this approach using the full-electron LAPW+lo method in the all-electron `exciting` package. Our results elucidate the role of many-body effects in shaping ultrafast excitonic processes in two-dimensional materials, contributing to the fundamental understanding necessary for optoelectronic and photonic applications.

I. INTRODUCTION

Due to the rapid development of the laser facilities, particularly their ability to generate ultrashort intense pulses [1], the study of real-time out-of-equilibrium electron dynamics has received significant attention [2–4]. Today, it is possible to observe electron dynamics on their natural attosecond timescale. In many light-matter interaction experiments with solids, excitonic effects, which stem from the strong Coulomb interaction between an electron in the conduction band (CB) and a hole in the valence band (VB), can play an essential role in charge dynamics. These effects are particularly prominent in non-metallic two-dimensional (2D) materials, where the attractive Coulomb interaction is less suppressed by screening. This can lead to excitonic binding energies of about 1 eV [5], which makes excitons stable at room temperature. Despite extensive research, the fundamental mechanisms underlying exciton formation and dynamics, particularly in the nonlinear response regime, are still not well understood.

Understanding these complex excitonic dynamics requires advanced experimental and theoretical approaches. Among these approaches, ultrafast spectroscopic techniques have emerged as powerful tools for probing the real-time behavior of electrons in materials. Most of the commonly used ultrafast techniques rely on a pump-probe scheme. A pump laser pulse, with a photon energy ranging from a tenth of an eV to several

eV excites a target, initiating transient charge dynamics that are subsequently probed by a second pulse. Techniques such as attosecond transient absorption spectroscopy (ATAS), X-ray absorption spectroscopy (XAS), angle-resolved photoemission spectroscopy (ARPES), and transient absorption spectroscopy (TR-abs) can be implemented in a time-resolved manner by controlling the pump-probe delay [6]. Another widely used technique is high-frequency light produced by pump-driven charge dynamics, known as solid-state high harmonic generation (sHHG) [7]. It has been shown that excitonic effects can significantly impact sHHG, if present [8]. A pump-probe setup inherently involves a nonlinear response due to interaction with two light pulses. Even a pump pulse itself can be intense enough to induce nonlinear effects. Therefore, a comprehensive theoretical description of these experiments should ideally account for light-matter interaction beyond the first order.

Excitonic effects can be incorporated using various real-time methods such as the propagation of the nonequilibrium Green's function [9–15], non-adiabatic RT-TDDFT [16–19], real-time propagation of the Bethe-Salpeter equation (BSE) [20], semiconductor Bloch equations [8, 21, 22], and time-dependent Hartree-Fock (TDHF) simulations [23]. In the frequency space, a target's nonlinear response can be studied using the lowest-nonzero-order perturbation theory with the solutions of the BSE [24–28]. While these methods provide complementary routes to describe excitonic effects, they differ significantly in computational cost, scalability, and ease of integration with existing electronic-structure frameworks.

To account for excitonic effects alongside the non-

* dm.tumakov@gmail.com

† daria.gorelova@b-tu.de

linear response to a laser field, we adopt the effective Schrödinger equation approach, suggested in Ref. [29]. We choose this framework because it provides a computationally efficient real-time scheme that retains the key many-body physics of the BSE while avoiding the explicit propagation of two-particle Green's functions or the full BSE kernel in time. This method utilizes nonequilibrium Berry-phase coupling with an external field [30] following the “modern theory of polarization” [31, 32]. It incorporates dynamical electron-hole interaction effects via the many-body perturbation theory (MBPT)-derived self-energy operator [9, 29, 33]. This technique, which combines the adaptability of a real-time approach with the natural ability of MBPT to capture electron correlation, has been successfully used for nonlinear response calculations [29, 34–37]. Its numerical implementation is available in the open-source YAMBO code, which uses a plane wave basis and pseudopotential approach [38, 39].

Here, we implement this functionality in the real-time time-dependent density functional theory (RT-TDDFT) module of the all-electron `exciting` package [40–42], which uses the linearized augmented plane-wave plus local orbitals (LAPW+lo) basis set. This basis set enables an accurate description of both delocalized and localized electronic states. LAPW+lo provides a highly precise numerical scheme for solving the Kohn-Sham equations [40]. In addition to improved accuracy, it allows for the future description of ultrafast XAS experiments due to its accurate treatment of core electrons.

We present a detailed theoretical study of the real-time charge dynamics of a 2D hexagonal boron nitride (h-BN) monolayer exposed to an ultrashort laser pulse using our highly accurate implementation. This prototype 2D material is often nicknamed as “white graphene” due to its similar lattice structure [43]. This insulator with a wide gap of $\sim 6\text{--}7$ eV [44–46] has been extensively studied both theoretically and experimentally over the decades due to its high thermal and chemical stability, as well as its optoelectrical properties [8, 47–55]. We study a resonant exciton formation by one- and two-photon absorption and describe the resulting dynamics. Another system we consider is a germanium monosulfide (GeS) monolayer, which has a moderate band gap of ~ 2.3 eV and a large predicted carrier mobility [56], making it promising for various photoelectric applications [56–58].

The paper is organized as follows. Section II describes the theoretical method used in detail. Section III provides details on the numerical implementation. The results of our calculations are presented in Section IV. Section V contains the concluding remarks.

II. THEORY

In this section, we summarize the real-time approach developed in Refs. [29, 30], which we implement in the `exciting` code, and employ in our calculations.

A. Real-time equations of motion

The dynamical macroscopic polarization along the lattice vector \mathbf{a}_α ($\alpha = 1, 2, 3$) obtained within the modern theory of polarization [30–32] is given by

$$\mathbf{P}_\alpha = \frac{f\mathbf{a}_\alpha}{2\pi V N_{\mathbf{k}_\alpha^\pm}} \sum_{\mathbf{k}_\alpha^\pm} \text{Im} \ln \prod_{i=1}^{N_{\mathbf{k}_\alpha^\pm}-1} \det S^{\mathbf{k}_i, \mathbf{k}_i^\pm}, \quad (1)$$

$$S_{mn}^{\mathbf{k}, \mathbf{k}_\alpha^\pm} = \langle v_{\mathbf{k}m} | v_{\mathbf{k}_\alpha^\pm n} \rangle. \quad (2)$$

Here, V is the unit cell volume, f is the spin degeneracy factor equal to two in this study, and $N_{\mathbf{k}_\alpha}$ is the number of equally distributed \mathbf{k} points along the reciprocal lattice vector \mathbf{b}_α , such that $\mathbf{a}_\alpha \cdot \mathbf{b}_\alpha = 2\pi$. $N_{\mathbf{k}_\alpha^\pm}$ is the number of \mathbf{k} points in the plane orthogonal (in lattice coordinates) to \mathbf{b}_α , $\mathbf{k}_\alpha^\pm = \mathbf{k} \pm \Delta\mathbf{k}_\alpha$, and $\Delta\mathbf{k}_\alpha = \mathbf{b}_\alpha/N_{\mathbf{k}_\alpha}$. We use atomic units (a.u.), $\hbar = m_e = -e = 1$, for this and the following equations. The time-dependent functions $v_{\mathbf{k}m}$ are the spatially periodic parts of the time-dependent Kohn-Sham-Bloch states $\phi_{\mathbf{k}m}(\mathbf{r}, t)$:

$$\phi_{\mathbf{k}m}(\mathbf{r}, t) = e^{i\mathbf{k}\cdot\mathbf{r}} v_{\mathbf{k}m}(\mathbf{r}, t), \quad v_{\mathbf{k}m}(\mathbf{r} + \mathbf{R}, t) = v_{\mathbf{k}m}(\mathbf{r}, t), \quad (3)$$

where \mathbf{R} is a Bravais lattice vector. Matrix $S^{\mathbf{k}_i, \mathbf{k}_i^\pm}$ is defined in Eq. (2) for a fixed spin projection. We restrict the consideration to the spin-symmetric case.

The Lagrangian for an infinite system with a uniform grid of $N_{\mathbf{k}}$ \mathbf{k} -points in the Brillouin zone (BZ) in the presence of a classical homogeneous electric field $\mathbf{E}(t)$ reads

$$L = \frac{1}{N_{\mathbf{k}}} \sum_{n, \mathbf{k}} [i \langle v_{\mathbf{k}n} | \dot{v}_{\mathbf{k}n} \rangle - \langle v_{\mathbf{k}n} | H_{\mathbf{k}}^0 | v_{\mathbf{k}n} \rangle] + V \mathbf{E}(t) \cdot \mathbf{P}(t), \quad (4)$$

where $\mathbf{P}(t)$ is the total macroscopic polarization, $\mathbf{P}(t) = \sum_\alpha \mathbf{P}_\alpha(t)$. The Euler-Lagrange equations for the Lagrangian (4) can be recast as the following equations of motion for the periodic parts of the Bloch states:

$$i \frac{d}{dt} v_{\mathbf{k}m}(t) = [H_{\mathbf{k}}^0 + V_{\mathbf{k}}^{\text{ext}}(t)] v_{\mathbf{k}m}(t), \quad (5)$$

$$H_{\mathbf{k}}^0 = e^{-i\mathbf{k}\cdot\mathbf{r}'} H^0 e^{i\mathbf{k}\cdot\mathbf{r}}, \quad (6)$$

where H^0 is the field-free system's Hamiltonian, \mathbf{r}' and \mathbf{r} correspond to the coordinates of the bra- and ket-states

respectively, and $V_{\mathbf{k}}^{\text{ext}}(t)$ is the operator describing the interaction with the external electromagnetic field:

$$V_{\mathbf{k}}^{\text{ext}}(t) = w_{\mathbf{k}}(\mathbf{E}(t)) + w_{\mathbf{k}}^{\dagger}(\mathbf{E}(t)), \quad (7)$$

$$w_{\mathbf{k}}(\mathbf{E}(t)) = \frac{i}{4\pi} \sum_m \sum_{\alpha=1}^3 (\mathbf{a}_{\alpha} \cdot \mathbf{E}(t)) N_{\mathbf{k}_{\alpha}} \sum_{\sigma=\pm} \sigma |\tilde{v}_{\mathbf{k}_{\alpha}^{\sigma} m}\rangle \langle v_{\mathbf{k}m}|, \quad (8)$$

where

$$\tilde{v}_{\mathbf{k}_{\alpha}^{\pm} m} = \sum_n \left[S^{\mathbf{k}, \mathbf{k}_{\alpha}^{\pm}} \right]_{nm}^{-1} v_{\mathbf{k}_{\alpha}^{\pm} n}. \quad (9)$$

We note that for any m , $w_{\mathbf{k}}^{\dagger}(\mathbf{E}(t)) |v_{\mathbf{k}m}(t)\rangle = 0$, and the second term in Eq. (7) is included only to ensure that the resulting operator is Hermitian. It can be shown that the one-particle density matrix constructed with the solutions of Eq. (5) as

$$\rho(\mathbf{r}, \mathbf{r}'; t) = \Omega^{-1} \sum_{m=1}^{n_{\text{occupied}}} \int_{\text{BZ}} d\mathbf{k} \phi_{\mathbf{k}m}(\mathbf{r}, t) \phi_{\mathbf{k}m}^*(\mathbf{r}', t) \quad (10)$$

evolves according to the Liouville–von Neumann equation [30]. Here, Ω is the BZ volume and the index m runs over n_{occupied} initially occupied states in the valence band (VB).

With the time-dependent functions $v_{\mathbf{k}m}(t)$ and, thus, the time-dependent overlap matrix (2), the macroscopic polarization can be obtained using Eq. (1). After time propagation, macroscopic response properties can be extracted from the time-dependent polarization vector $\mathbf{P}(t)$.

We assume the dipole approximation for the classical electromagnetic field $\mathbf{E}(t)$, which is switched on at some time $t_0 \geq 0$. Within this approximation, the electric field is spatially uniform, thus only vertical optical transitions are possible, and no magnetic field effects are present. This approximation is well established for the moderate field strengths and relatively long wavelengths used in our calculations.

All post excitation relaxation processes such as carrier cooling, scattering, transport, and recombination [59] are neglected in our study, as we focus on the first few tens of femtoseconds following the excitation.

B. Electron-electron dynamic interaction

We define the explicitly field-free Hamiltonian as

$$H^0 \equiv H^{\text{GS}} + \delta V^{\text{ee}}[\rho(t)], \quad (11)$$

where δV^{ee} contains a time-dependent correction to the inter-electronic interaction. The ground-state (GS) Hamiltonian reads

$$H^{\text{GS}} = T + V^{\text{nucl}} + V^{\text{H}}[\rho(0)] + V^{\text{xc}}[\rho(0)] + \Delta H^{\text{QP}}, \quad (12)$$

where T is the total one-particle kinetic energy operator, V^{nucl} describes the interaction with static nuclei, V^{H} is the Hartree potential responsible for the local field effects [60], V^{xc} is the local KS exchange-correlation potential, and ΔH^{QP} is the state-dependent scissor operator [61, 62] rigidly shifting the CB on the value ΔE^{QP} upwards:

$$\Delta H^{\text{QP}} = \Delta E^{\text{QP}} \sum_{m \in \text{CB}} \psi_{\mathbf{k}m}(\mathbf{r}') \psi_{\mathbf{k}m}^*(\mathbf{r}). \quad (13)$$

The value of ΔE^{QP} can be chosen from experimental data or results of GW calculations present in literature. In the simulations, we compare different levels of accuracy to account for the dynamic electron-electron interaction. The first level is the independent particle approximation (IPA), with the effective KS potential being fixed to its unperturbed ground-state value:

$$\delta V^{\text{ee,IPA}}[\rho(t)] = 0. \quad (14)$$

The electron-hole interaction effects are incorporated using the time-dependent adiabatic GW (TD-a GW) approximation (also referred to as the time-dependent Hartree + Screened EXchange (HSEX) approximation):

$$\delta V^{\text{ee,aGW}}[\rho] = V^{\text{H}}[\rho(t)] - V^{\text{H}}[\rho(0)] + \delta V^{\text{ee,SEX}}[\rho(t)], \quad (15)$$

where the self energy is obtained within the SEX (Screened EXchange) [63–65] approximation:

$$\delta V^{\text{ee,SEX}}[\rho(t)] = \Sigma^{\text{SEX}}[\rho(t)] - V^{\text{xc}}[\rho(0)]. \quad (16)$$

Self energy term, which is time-dependent through the time-dependent density matrix, is defined as:

$$\Sigma^{\text{SEX}}[\rho(t)] = -\rho(t) W_0(\mathbf{r}, \mathbf{r}'; \omega = 0), \quad (17)$$

where W_0 is the static (instantaneous) limit of the dynamically screened Coulomb interaction, which can be obtained in the reciprocal space:

$$W_0(\mathbf{r}, \mathbf{r}') = \sum_{\mathbf{G}\mathbf{G}'\mathbf{q}} e^{i(\mathbf{G}+\mathbf{q})\mathbf{r}} \varepsilon_{\mathbf{G}\mathbf{G}'}^{-1}(\mathbf{q}) v(\mathbf{q}+\mathbf{G}')(\mathbf{q}) e^{-i(\mathbf{G}'+\mathbf{q})\mathbf{r}'}, \quad (18)$$

$$\varepsilon_{\mathbf{G}\mathbf{G}'}(\mathbf{q}) = \delta_{\mathbf{G}\mathbf{G}'} - v(\mathbf{q}+\mathbf{G}) \chi_{\mathbf{G}\mathbf{G}'}(\mathbf{q}), \quad (19)$$

where the bare Coulomb potential reads

$$v(\mathbf{q}) = 4\pi/q^2. \quad (20)$$

The polarizability $\chi_{\mathbf{G}\mathbf{G}'}(\mathbf{q})$ is constructed within the random phase approximation (RPA):

$$\chi_{\mathbf{G}\mathbf{G}'}(\mathbf{q}) = \sum_{nn'\mathbf{k}} M_{\mathbf{G}n'n}^{\mathbf{k}+\mathbf{q}\mathbf{k}} M_{\mathbf{G}'n'n}^{\mathbf{k}+\mathbf{q}\mathbf{k}} \frac{f(\epsilon_{\mathbf{k}+\mathbf{q}n'}) - f(\epsilon_{\mathbf{k}n})}{\epsilon_{\mathbf{k}+\mathbf{q}n'} - \epsilon_{\mathbf{k}n}}, \quad (21)$$

where $f(\epsilon_{\mathbf{k}n})$ are the occupation numbers, and

$$M_{\mathbf{G}p n}^{\mathbf{k}\mathbf{k}'} = \int d\mathbf{r} \psi_{\mathbf{k}p}^*(\mathbf{r}) e^{i(\mathbf{G}+\mathbf{k}-\mathbf{k}')\cdot\mathbf{r}} \psi_{\mathbf{k}'n}(\mathbf{r}). \quad (22)$$

The TD-aGW approximation reduces to the BSE in the linear response limit [9].

Since we employ the length gauge for the external field coupling, non-local operators such as the scissor correction or the self-energy operator can be added directly to the Hamiltonian without any complications specific for the velocity gauge. Namely, the operators do not need to be gauge-transformed, and the velocity operator does not need to be redefined [66].

C. Electric field strength limitations

Despite the field coupling term being non-perturbative, there are still limitations on the peak field strength. Due to Zener tunneling, the operator (7) becomes unbounded from below [67] at a critical field amplitude \mathbf{E}^{crit} , which can be estimated as [68]:

$$|\mathbf{E}^{\text{crit}} \cdot \mathbf{a}_\alpha| = \frac{E_{\text{gap}}}{N_{\mathbf{k}_\alpha}}, \quad (23)$$

where E_{gap} is a fundamental gap. In all calculations presented here, the field strength does not exceed a few percent of this critical value. Another limitation arises from the approximation employed for the self-energy operator: neglecting its explicit time dependence is only valid when the excitonic density n_{exc} remains below the Mott transition threshold [26, 69, 70]. This threshold can be estimated using the exciton's characteristic coordinate-space size r_{exc} as $n_{\text{exc}} \sim r_{\text{exc}}^{-d}$ with d being the system's dimensionality.

III. IMPLEMENTATION DETAILS

In the simulations, we expand the time-dependent states $v_{\mathbf{k}n}(t)$ with the set of the periodic parts of the ground state Kohn-Sham-Bloch orbitals:

$$v_{\mathbf{k}n}(t) = \sum_m c_{\mathbf{k}mn}(t) u_{\mathbf{k}m}, \quad (24)$$

where the time-independent functions $u_{\mathbf{k}m}$ are defined by

$$\psi_{\mathbf{k}m}(\mathbf{r}) = e^{i\mathbf{k}\cdot\mathbf{r}} u_{\mathbf{k}m}(\mathbf{r}), \quad u_{\mathbf{k}m}(\mathbf{r} + \mathbf{R}) = u_{\mathbf{k}m}(\mathbf{r}), \quad (25)$$

$$H^0 \psi_{\mathbf{k}m} = \epsilon_{\mathbf{k}m} \psi_{\mathbf{k}m}, \quad m = 1, \dots, N. \quad (26)$$

The value of $N = n_{\text{occupied}} + n_{\text{empty}}$ is defined by the number n_{empty} of initially unoccupied conduction band (CB) states included in the basis set. Substituting the

expansion (24) into Eq. (5), we obtain the following equation for the expansion coefficients:

$$i \frac{d}{dt} c_{\mathbf{k}pn}(t) = \sum_m [\langle u_{\mathbf{k}p} | H_{\mathbf{k}}^0 + V_{\mathbf{k}}^{\text{ext}}(t) | u_{\mathbf{k}m} \rangle] c_{\mathbf{k}mn}(t). \quad (27)$$

We set $c_{\mathbf{k}pn}(0) = \delta_{pn}$ for each \mathbf{k} and p as the initial condition for Eqs. (27). The set of matrix differential equations (27) is evolved in time using the 4th-order Runge-Kutta method (RK4) available in the `exciting` package [41].

As the functions $v_{\mathbf{k}m}(t)$ are constructed and evolved numerically independently for different \mathbf{k} points, they acquire independently a random initial phase. By construction, the operator in Eq. (7), which couples neighboring \mathbf{k} points, is gauge-covariant and satisfies the Born-von Karman periodic boundary conditions [30]. Eq. (8) implies a two-point finite-difference approximation for the derivative in \mathbf{k} space. Achieving a higher level of accuracy is possible by applying it twice, with step sizes of $\Delta\mathbf{k}_\alpha$ and $2\Delta\mathbf{k}_\alpha$, provided there are at least five \mathbf{k} points along the \mathbf{b}_α direction [71]:

$$w_{\mathbf{k}} = \frac{1}{3} (4w_{\mathbf{k}}|_{\Delta\mathbf{k}_\alpha} - w_{\mathbf{k}}|_{2\Delta\mathbf{k}_\alpha}). \quad (28)$$

To reduce the computational cost, we assume that n_{frozen} lowest-lying valence states for each \mathbf{k} point are irrelevant for a specific process under consideration, and only propagate $n_{\text{active}} = n_{\text{occupied}} - n_{\text{frozen}}$ states, i.e. $c_{\mathbf{k}mn}(t) = \delta_{mn}$ for $n = 1, \dots, n_{\text{frozen}}$. The results are checked for convergence both with decreasing n_{frozen} and increasing n_{empty} .

The details of evaluation of the local operators' matrix elements in the `exciting` package can be found in Ref. [40]. The field coupling matrix $\langle u_{\mathbf{k}p} | V_{\mathbf{k}}^{\text{ext}}(t) | u_{\mathbf{k}m} \rangle$ involves a time-dependent overlap between states from different \mathbf{k} points:

$$S_{ln}^{\mathbf{k}, \mathbf{k}_\alpha^\sigma}(t) = \sum_p c_{\mathbf{k}pl}^*(t) G_{pn}^{\mathbf{k}\mathbf{k}_\alpha^\sigma}(t), \quad (29)$$

where

$$G_{pn}^{\mathbf{k}\mathbf{k}_\alpha^\sigma}(t) = \sum_r \langle u_{\mathbf{k}p} | u_{\mathbf{k}_\alpha^\sigma r} \rangle c_{\mathbf{k}_\alpha^\sigma rn}(t). \quad (30)$$

This introduces real-time communication between different MPI (Message Passing Interface) processes when \mathbf{k} -grid parallelization is employed. For all $\alpha = 1, 2, 3$ and $\sigma = \pm 1, \pm 2$, we keep the time-independent $n_{\text{occupied}} \times n_{\text{occupied}}$ matrix $\langle u_{\mathbf{k}p} | u_{\mathbf{k}_\alpha^\sigma r} \rangle$ available on the MPI process controlling the point \mathbf{k} . In this way, communication is reduced to an inexpensive exchange of $(n_{\text{occupied}} + n_{\text{empty}}) \times n_{\text{active}}$ matrices of the coefficients $c_{\mathbf{k}rn}(t)$. The matrix

$$\langle u_{\mathbf{k}m} | u_{\mathbf{k}_\alpha^\sigma n} \rangle = \int \psi_{\mathbf{k}m}^*(\mathbf{r}) e^{-i(\mathbf{k}_\alpha^\sigma - \mathbf{k})\cdot\mathbf{r}} \psi_{\mathbf{k}_\alpha^\sigma + \mathbf{s}\mathbf{b}_\alpha n}(\mathbf{r}) d\mathbf{r}, \quad (31)$$

where $s = 0, \pm 1$ depending on whether the neighboring \mathbf{k} points lie in the same Brillouin zone, is calculated just once prior to the time propagation. The Hartree potential matrix $\langle \psi_{\mathbf{k}p} | V^H[\rho(t)] | \psi_{\mathbf{k}m} \rangle$ is evaluated in the linearized augmented plane wave and local orbitals (LAPW+lo) basis set employed in the `exciting`, and then transformed to the KS basis.

For the efficient real-time recalculation of the dynamical interelectronic interaction potential, we adopt the approach employed in the YAMBO code [9]. First, we precalculate the four-point matrix

$$\mathcal{W}_{pmnl}^{kk'} = \sum_{GG'} W_{GG'}(\mathbf{k} - \mathbf{k}') M_{Gpn}^{kk'} \left(M_{G'ml}^{kk'} \right)^*. \quad (32)$$

Then, the matrix elements of the self-energy operator are obtained at each time propagation step as

$$\langle \psi_{\mathbf{k}p} | \Sigma^{\text{SEX}} | \psi_{\mathbf{k}m} \rangle = - \sum_{nl\mathbf{k}'} \mathcal{W}_{pmnl}^{kk'} \sum_{s=1}^{n_{\text{occupied}}} c_{\mathbf{k}ns}(t) c_{\mathbf{k}ls}^*(t). \quad (33)$$

We work within the following approximation: in the summation in Eq. (33), we only include terms where the pairs p, n and m, l lie within the same band. Omitting the remaining terms is not expected to affect our results [26]. For the details of calculation of the matrix $\mathcal{W}_{pmnl}^{kk'}$, which is the direct interaction term in BSE, in `exciting`, please refer to Ref. [72].

Finally, we would like to make a remark regarding the evaluation of the macroscopic polarization. Contributions from different ‘‘strings’’ (i.e., $N_{\mathbf{k}_\alpha^\perp}$ sets of \mathbf{k} points along the direction α) in Eq. (1) must have consistent phases before averaging over \mathbf{k}_α^\perp . To ensure that no random branch jumps occur during the propagation, we match the string phases at times t and $t + \Delta t$ at each time step.

IV. RESULTS AND DISCUSSION

A. Ground state and linear response

For both h-BN and GeS crystals, we start with the calculation of the ground KS state with the local DFT exchange-correlation functional $V^{\text{xc}}[\rho]$ within the Perdew-Burke-Ernzerhof generalized gradient approximation revised for solids (GGA-PBESol) [73]. We then obtain the macroscopic dielectric function $\varepsilon_{ij}(\omega) = \delta_{ij} + 4\pi P_i(\omega)/E_j(\omega)$ by performing a real-time simulation. The external field $\mathbf{E}(t) = E(t)\mathbf{e}_j$ is chosen to be the Dirac delta function $E(t) = E_0\delta(t - t_0)$, so that the pulse is flat in the frequency space, $E(\omega) = \text{const.}$ At the postprocessing stage, we include the broadening parameter $\omega_{\text{cut}} = 0.1$ eV when evaluating the Fourier transform of the time-dependent polarization, $\mathbf{P}(\omega) =$

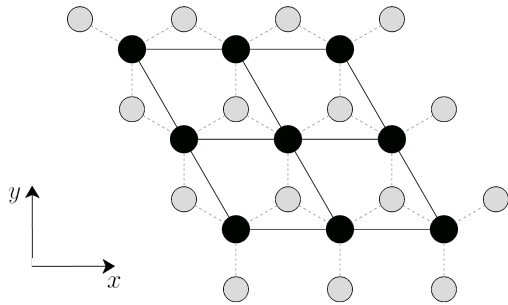


FIG. 1: Scheme of the considered orientation of the honeycomb h-BN structure in real space. Unit cells are shown with solid black lines. Black circles represent B atoms, and gray circles represent N atoms.

$\int e^{-i(\omega - i\omega_{\text{cut}})t} \mathbf{P}(t) dt$, to mimic the experimental spectral broadening.

1. h-BN monolayer

Figure 1 shows the structure and considered orientation of the h-BN monolayer. The two-dimensional unit cell vectors are $a \cdot (1, 0)$ and $a \cdot (-1/2, \sqrt{3}/2)$, where the lattice constant and the nearest-neighbor distance between atoms of the same species is $a = 2.51 \text{ \AA}$ (~ 4.74 a.u.).

We choose a two-dimensional \mathbf{k} grid of 60×60 points equally distributed over the Brillouin zone. To mimic the direct GW quasiparticle gap of 7.25 eV [74] located at the K point, we apply a quasiparticle scissor correction as defined in Eq. (13) of $\Delta E^{\text{QP}} = 2.62$ eV. Figure 2a shows the band structure and partial density of states (PDOS) obtained with the ground state Hamiltonian (12). Near the gap, valence states are essentially concentrated on N sites, which agrees with the literature [26, 48].

Only the lowest CB states and the highest-lying VB states are expected to be involved in the dynamics with the laser field parameters we are using. Therefore, we set the number of states in the CB $n_{\text{empty}} = 2$ and consider two highest-lying VB states for each \mathbf{k} point, when performing the time propagation. In the actual calculations, only the two highest-lying states are evolved in time ($n_{\text{active}} = 2$), while the other states remain fixed at their initial values.

We present the simulation results for $\text{Im}\varepsilon(\omega)$ in Fig. 2b, where $\varepsilon_{xx}(\omega) = \varepsilon_{yy}(\omega) \equiv \varepsilon(\omega)$ due to the symmetry of the system. Three excitonic peaks (marked by a, b and c) are clearly visible within the gap defined by the scissor-shifted IPA-level response. Based on the symmetries of the corresponding excitonic wavefunctions obtained with the solutions of the BSE, these peaks can be attributed to the $1s$ -, $2p$ - and $2s$ -like states, respec-

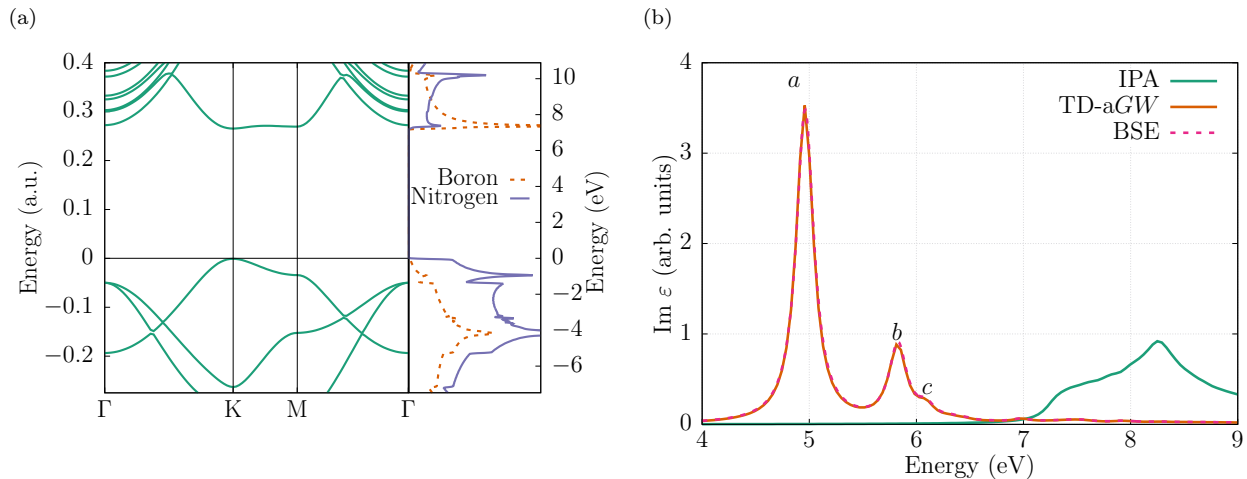


FIG. 2: (a) Band structure and partial density of states of the h-BN monolayer in the ground state obtained within the DFT framework. The conduction band is shifted 2.62 eV upwards via the scissor operator (13) to mimic the GW quasiparticle gap. (b) Imaginary part of the dielectric function $\text{Im } \varepsilon$ of an h-BN monolayer calculated with time-domain response to the delta-shaped pulse. The IPA curve was obtained within the independent particle approximation (Eq. (14)), while the TD-aGW curve is obtained with the full Hamiltonian (15). The dashed BSE curve is obtained with the BSE. Lorentzian broadening of 0.1 eV is included in the postprocessing-stage Fourier transform.

tively [22, 48, 55, 74]. We note that while the shape of the peaks is fully converged, a finer \mathbf{k} -grid is required to determine peak positions with more than about 0.3 eV accuracy achieved here. However, these positions can be adjusted using the scissor operator. The point symmetry group of h-BN is D_{3h} with six irreducible representations: A'_1 , A'_2 , E' , A''_1 , A''_2 and E'' . Since the in-plane electric dipole transition operator belongs to E' , only E' states are visible in the linear response [36, 75], and two additional excitonic $2p$ -like states belonging to A'_2 and A'_1 are dark [48].

We also compare the linear response dielectric function with the one obtained from the direct solution of the BSE using the `exciting` code. As expected [9], the BSE curve is almost indistinguishable from the TD-aGW one.

2. GeS monolayer

Figure 3 shows the structure and the considered orientation of the GeS monolayer. The unit cell is formed by the orthogonal vectors $a_x \cdot (1, 0)$ and $a_y \cdot (0, 1)$ with the lattice constants $a_x = 4.43 \text{ \AA}$ (~ 8.37 a.u.) and $a_y = 3.67 \text{ \AA}$ (~ 6.94 a.u.). Atom positions in the lattice coordinates are set to (0.631, 0.5, 0.986) and (0.131, 0, 0.120) for Ge; and (0, 0, 0) and (0.5, 0.5, 0.106) for S. The geometry parameters are taken from the Ref. [58]. For the GeS monolayer, we use 40×40 \mathbf{k} grid. A scissor shift ΔE^{QP} is set to 1.07 eV to mimic the quasiparticle gap of 2.72 eV [58]. The calculated band structure and the corresponding PDOS are shown in Fig. 4a. Since the PDOS in the considered energy range is nearly identical

for atoms of the same species, the displayed PDOS is summed over all atoms of each species.

In the real-time simulations, we only evolve two highest-lying VB states, and choose $n_{\text{empty}} = 2$ in the CB. Figure 4b we shows the linear response spectrum with three clearly visible excitonic peaks.

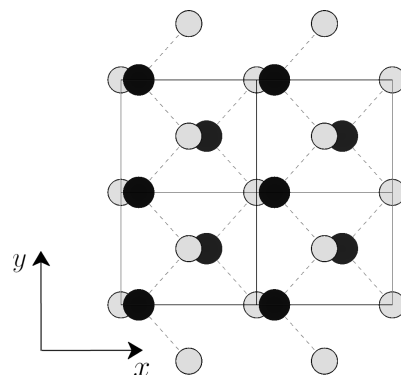


FIG. 3: Scheme of the considered orientation of the GeS monolayer in real space. Unit cells are shown with solid black lines. Black circles represent Ge atoms, and gray circles represent S atoms. Direction x is the “armchair” direction, and y is the “zigzag” one.

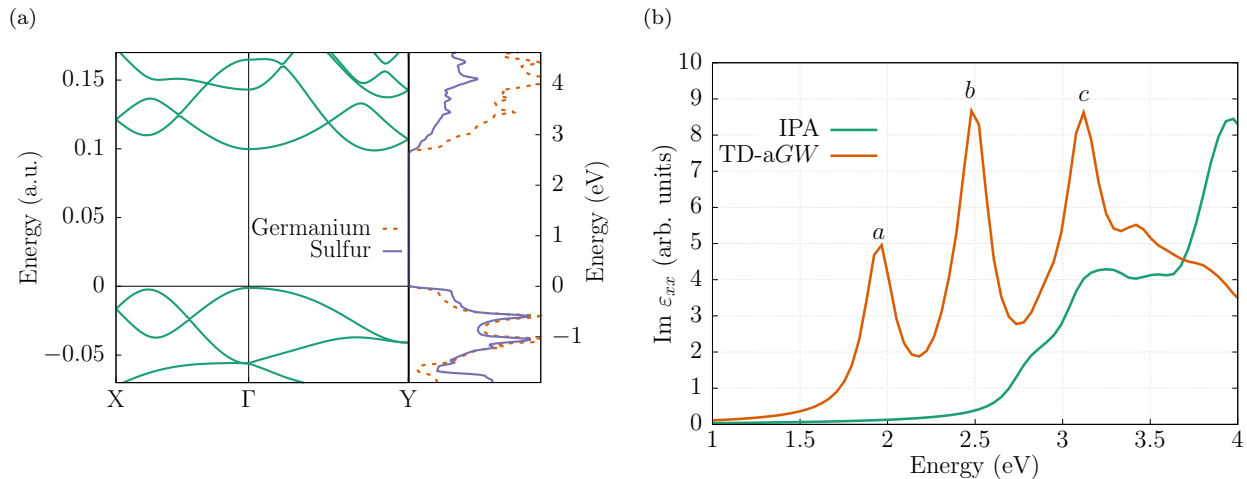


FIG. 4: (a) Band structure and partial density of states of the GeS in the ground state obtained within the DFT framework. The conduction band is shifted by 1.07 eV upwards via the scissor operator (13) to mimic the GW quasiparticle band gap. (b) Imaginary part of the dielectric function $\text{Im } \varepsilon_{xx}$ of a GeS monolayer calculated with time-domain response to the delta-shaped pulse. The IPA curve was obtained within the independent particle approximation (Eq. (14)), while the TD-aGW curve is obtained with the full Hamiltonian (15). Lorentzian broadening of 0.1 eV is included in the postprocessing-stage Fourier transform. Direction x is the “armchair” direction of a GeS monolayer.

B. Real-time charge dynamics

For the real-time calculations, we assume a laser pulse with a \sin^2 -shaped time-dependent vector potential and different other parameters which are specified below.

1. h -BN monolayer

The authors of Ref. [22] studied a light-induced charge migration in a scenario where both $2s$ and $2p$ excitons are excited by a single circularly-polarized pulse, using the tight-binding (TB) model. They showed that such excitation results in quantum beats in the electric current, corresponding to the charge migration between $2s$ and $2p$ excitonic states in both momentum and coordinate spaces. To see our implementation in action, and to verify whether this behavior persists beyond the TB simulations, and under less symmetrical (i.e. linearly-polarized) perturbation, we set the laser pulse intensity to approximately 10^{10} W/cm², pulse duration to approximately 20 fs, and the central photon energy to ≈ 6.12 eV to excite both b and c excitons shown in Fig. 2a.

In Fig. 5a (top panel), we show our results for the time-dependent residual macroscopic polarization obtained using Eq. (1). One can clearly see the quantum beats pattern with a period of approximately 16 fs, related to the relative positions of the excitonic peaks b and c as $2\pi/16$ fs ≈ 0.25 eV.

In the top row of Fig. 5b, we present the \mathbf{k} -space CB occupations at the time moments indicated by the vertical lines in Fig. 5a, calculated as

$$\rho_{\mathbf{k}}(t) = \sum_{m=1}^{n_{\text{occupied}}} \sum_{n \in \text{CB}} |\langle \phi_{\mathbf{k}m}(\mathbf{r}, t) | \phi_{\mathbf{k}n}(\mathbf{r}, t=0) \rangle|^2. \quad (34)$$

Based on the analysis of the BSE solutions obtained in Ref. [48], the left and the right distributions can be attributed to the $2s$ and $2p$ - E' excitonic states, respectively, with the symmetry being partially broken by the y -polarized laser pulse. For completeness, the bottom row of Fig. 5b shows the change in the state occupation relative to the ground state along the standard \mathbf{k} -path. We also observe charge migration in and out of the K point reported in Ref. [22]. Since the change in the charge density in real space involves integral contributions from all unit cells, the resulting distributions for both excitonic states look qualitatively the same: charge density oscillates between the B and N sites. Therefore, the real-space charge density plots are not shown here.

To include additional excitonic states in charge migration dynamics, we change the central photon energy of the laser field from 6.12 eV to 3.06 eV. Two photons are now necessary to excite the system resulting in a change in the selection rules. The two-photon process can also trigger the formation of the A'_1 exciton [75]. Since the two-photon process is much less probable than the one-photon one, we adjust the field peak amplitude to 10^{11} W/cm² to achieve the CB population comparable to the previous case of around 10^{-3} excitations per unit cell.

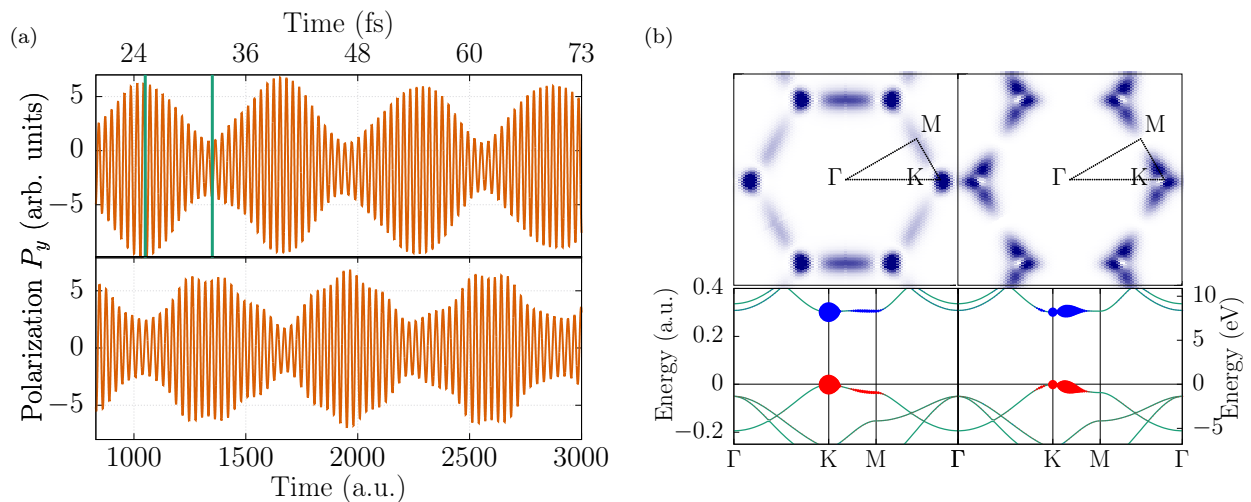


FIG. 5: (a) Time-dependent macroscopic residual polarization P_y in an h-BN monolayer after excitation by a linearly-polarized, \sin^2 -shaped pulse with a central photon energy of 6.12 eV (top panel), 3.06 eV (bottom panel), and a duration of 830 a.u. (≈ 21 fs). On the top panel, vertical dashed lines mark the moments in time, when the time-dependent excitonic state is almost $2s$ -like (left line), and $2p$ -like (right line). (b) Top row: conduction band occupations in an h-BN monolayer after excitation by the short linearly-polarized pulse with a central photon energy 6.12 eV at $t \approx 25$ fs (left) and $t \approx 32.5$ fs (right) in reciprocal space. The selected time points correspond to the vertical lines in Fig. 5a. Bottom row: change in the occupations of unperturbed states along the standard \mathbf{k} -path at the same times. Red and blue colors indicate the positive and negative charge differences, respectively, while point size represents the magnitude of the change.

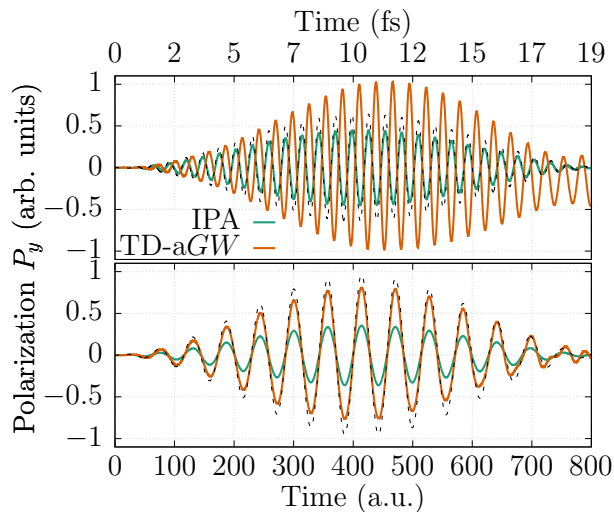


FIG. 6: Time-dependent macroscopic polarization P_y in an h-BN monolayer during excitation by a linearly-polarized, \sin^2 -shaped pulse with a central photon energy of 6.12 eV (top panel), 3.06 eV (bottom panel), and a duration of 830 a.u. (≈ 21 fs). (IPA) curve was obtained within the independent particle approximation (Eq. (14)), (TD-aGW) curve corresponds to the calculations with dynamical electron-hole interactions (Eq. (15)). Dashed line depicts the electric field strength.

The bottom panel of Fig. 5a shows the macroscopic polarization after a two-photon excitation. Although the transition energy is the same, the charge dynamics now involve more than two excitonic states, which distorts the beats pattern. We also observe that the phase of the polarization beating is shifted by $\pi/2$ relative to the linear-response one. Since the $2p-A'_1$ exciton appears nearly identical to the $2p-E'$ exciton in reciprocal space, [48] the occupations presented in Fig. 5b stay qualitatively the same in the two-photon scenario.

Finally, we show the “in-field” macroscopic polarization response in Fig. 6. The top panel corresponds to the one-photon case, while the bottom panel shows the two-photon response. We obtain the polarization both with (TD-aGW) and without (IPA) the self energy term, i.e. including and excluding electron-hole interactions. Since the central photon energy of the field is set below the IPA energy gap, transition probability is negligible within the independent particle picture. Thus, polarization follows the external field in both the linear and nonlinear regimes within this approximation. Due to excitonic effects, the transition probability is significant at a photon energy of 6.12 eV as can be seen in Fig. 2b. As a result, excitonic effects significantly impact the system’s response in the linear regime. Even when the field is present, the time-dependent polarization is dominated by the contribution due to electronic excitations. The non-zero imaginary

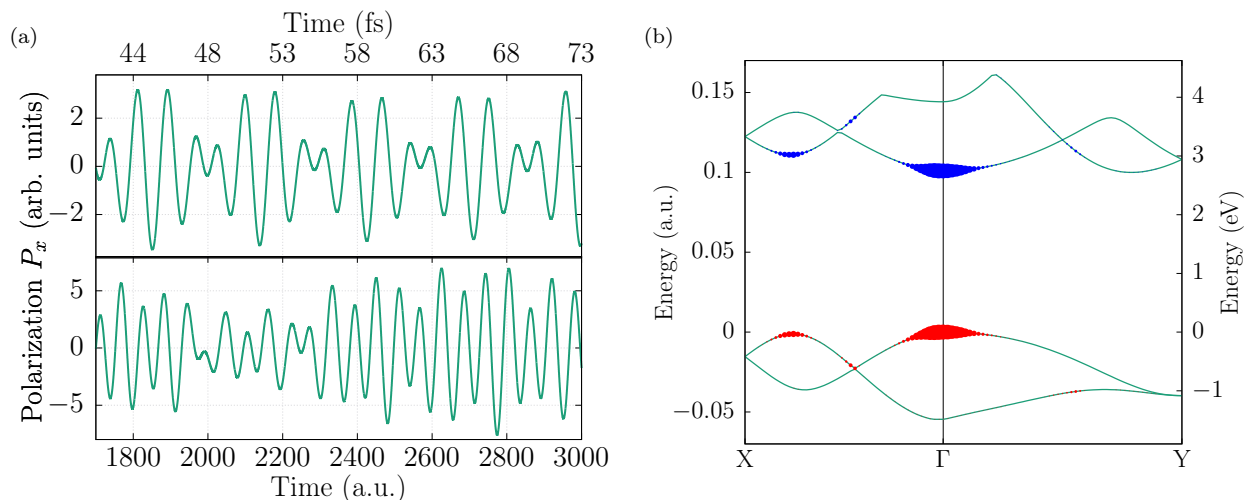


FIG. 7: (a) Time-dependent macroscopic polarization P_x in a GeS monolayer after excitation by a linearly-polarized, \sin^2 -shaped pulse with a central photon energy of 2.01 eV (top panel), 1 eV (bottom panel), and a duration of 1700 a.u. (≈ 41 fs). Direction x is the “armchair” direction of a GeS monolayer. (b) Change in the occupations of unperturbed states along the standard \mathbf{k} -path in an GeS monolayer after excitation by the short linearly-polarized pulse with a central photon energy 2.01 eV at $t \approx 48$ fs. Red and blue colors indicate the positive and negative occupation differences, respectively, while point size represents the magnitude of the change.

part of the dielectric function naturally manifests as a shift in oscillation phase. In the two-photon case, excitonic effects are naturally suppressed due to the dominance of the linear response.

2. GeS monolayer

In the case of a GeS monolayer, we set the laser pulse duration to approximately 41 fs. The central photon energy is set to 2.01 eV in the linear regime and to 1 eV in the nonlinear regime so that the two excitonic states marked by a and b in the Fig. 4b are excited. We choose the longer pulse to narrow the electric field’s Fourier transform in the frequency space, which better isolates the desired excitation.

The residual macroscopic polarization is shown in the Fig. 7a. As in the previous case, the clear pattern produced by the single-photon excitation is disturbed due to the dark state transition excited in the two-photon process.

Occupations along the standard \mathbf{k} path at $t \approx 78$ fs are shown in Fig. 7b. Since the energy difference between the excitonic states is comparable to their energy difference from the ground state, the time evolution does not exhibit beatings. Therefore, the moments, when only one of the a or b excitonic states contributes are not distinguishable. Instead, we observe the “trembling” distribution, in which both states are always present.

V. SUMMARY

We investigated exciton dynamics in two-dimensional h-BN and GeS monolayers exposed to an ultrashort laser pulse, using the RT-aGW approximation, capturing electron-hole correlations beyond the independent-particle picture. We implemented a highly accurate real-time propagation scheme based on the dynamical Berry phase approach to treat the coupling to time-dependent electric fields in the all-electron `exciting` package, employing the LAPW+lo basis set. Electron-hole interactions are incorporated through a non-local self-energy operator derived from the MBPT, which is equivalent to the BSE in the weak-field regime. Using our implementation, we studied response of the two-dimensional materials to an external field in linear and nonlinear regimes. We analyzed the impact of electron-hole interactions on electron dynamics during the action of a pump pulse. We demonstrated that they can result in different amplitudes and shifted phases of polarization compared to polarization calculated within the IPA. We also demonstrated the emergence of a quantum-beat scenario, which can be suppressed by breaking the symmetry of the driving field.

ACKNOWLEDGMENTS

This work has been supported by the Volkswagen Foundation grant number 96237.

- [1] N. Huang, H. Deng, B. Liu, D. Wang, and Z. Zhao, Features and futures of x-ray free-electron lasers, *The Innovation* **2**, 100097 (2021).
- [2] A. Zong, B. R. Nebgen, S.-C. Lin, J. A. Spies, and M. Zuerch, Emerging ultrafast techniques for studying quantum materials, *Nature Reviews Materials* **8**, 224 (2023).
- [3] M. Chergui, M. Beye, S. Mukamel, C. Svetina, and C. Masciovecchio, Progress and prospects in nonlinear extreme-ultraviolet and x-ray optics and spectroscopy, *Nature Reviews Physics* **5**, 578 (2023).
- [4] S. M. Cavaletto, K. M. Kowalczyk, F. O. Navarrete, and J. Rivera-Dean, The attoscience of strong-field-driven solids, *Nature Reviews Physics* , 1 (2024).
- [5] G. Wang, A. Chernikov, M. M. Glazov, T. F. Heinz, X. Marie, T. Amand, and B. Urbaszek, Colloquium: Excitons in atomically thin transition metal dichalcogenides, *Rev. Mod. Phys.* **90**, 021001 (2018).
- [6] A. Stolow, A. E. Bragg, and D. M. Neumark, Femtosecond time-resolved photoelectron spectroscopy, *Chemical Reviews* **104**, 1719 (2004), pMID: 15080710.
- [7] S. Ghimire and D. A. Reis, High-harmonic generation from solids, *Nature physics* **15**, 10 (2019).
- [8] E. B. Molinero, B. Amorim, M. Malakhov, G. Cistaro, Á. Jiménez-Galán, A. Picón, P. San-José, M. Ivanov, and R. E. Silva, Subcycle dynamics of excitons under strong laser fields, *Science Advances* **10**, eadn6985 (2024).
- [9] C. Attaccalite, M. Grüning, and A. Marini, Real-time approach to the optical properties of solids and nanostructures: Time-dependent bethe-salpeter equation, *Phys. Rev. B* **84**, 245110 (2011).
- [10] G. Stefanucci and R. Van Leeuwen, *Nonequilibrium many-body theory of quantum systems: a modern introduction* (Cambridge University Press, 2013).
- [11] E. Perfetto, D. Sangalli, A. Marini, and G. Stefanucci, Nonequilibrium bethe-salpeter equation for transient photoabsorption spectroscopy, *Phys. Rev. B* **92**, 205304 (2015).
- [12] E. Perfetto, D. Sangalli, M. Palumbo, A. Marini, and G. Stefanucci, First-principles nonequilibrium green's function approach to ultrafast charge migration in glycine, *Journal of Chemical Theory and Computation* **15**, 4526 (2019).
- [13] E. Ridolfi, P. E. Trevisanutto, and V. M. Pereira, Expedient computation of nonlinear optical properties of arbitrary order with native electronic interactions in the time domain, *Physical Review B* **102**, 245110 (2020).
- [14] D. Sangalli, Excitons and carriers in transient absorption and time-resolved arpes spectroscopy: An ab initio approach, *Physical Review Materials* **5**, 083803 (2021).
- [15] E. Perfetto, Y. Pavlyukh, and G. Stefanucci, Real-time gw: Toward an ab initio description of the ultrafast carrier and exciton dynamics in two-dimensional materials, *Physical Review Letters* **128**, 016801 (2022).
- [16] T. Sander and G. Kresse, Macroscopic dielectric function within time-dependent density functional theory—real time evolution versus the casida approach, *The Journal of Chemical Physics* **146**, 064110 (2017).
- [17] C. D. Pemmaraju, Simulation of attosecond transient soft x-ray absorption in solids using generalized kohn–sham real-time time-dependent density functional theory, *New Journal of Physics* **22**, 083063 (2020).
- [18] J. Sun, C.-W. Lee, A. Kononov, A. Schleife, and C. A. Ullrich, Real-time exciton dynamics with time-dependent density-functional theory, *Phys. Rev. Lett.* **127**, 077401 (2021).
- [19] J. R. Williams, N. Tancogne-Dejean, and C. A. Ullrich, Time-resolved exciton wave functions from time-dependent density-functional theory, *Journal of Chemical Theory and Computation* **17**, 1795 (2021).
- [20] X. Jiang, Q. Zheng, Z. Lan, W. A. Saidi, X. Ren, and J. Zhao, Real-time gw-bse investigations on spin-valley exciton dynamics in monolayer transition metal dichalcogenide, *Science Advances* **7**, eabf3759 (2021).
- [21] G. Cistaro, M. Malakhov, J. J. Esteve-Paredes, A. J. Uria-Álvarez, R. E. Silva, F. Martín, J. J. Palacios, and A. Picón, Theoretical approach for electron dynamics and ultrafast spectroscopy (edus), *Journal of Chemical Theory and Computation* **19**, 333 (2023).
- [22] M. Malakhov, G. Cistaro, F. Martín, and A. Picón, Exciton migration in two-dimensional materials, *Communications Physics* **7**, 196 (2024).
- [23] S. V. B. Jensen, L. B. Madsen, A. Rubio, and N. Tancogne-Dejean, High-harmonic spectroscopy of strongly bound excitons in solids, *Phys. Rev. A* **109**, 063104 (2024).
- [24] A. Rieger and W. G. Schmidt, Solving the bethe-salpeter equation for the second-harmonic generation in zn chalcogenides, *Phys. Rev. B* **96**, 235206 (2017).
- [25] C. Vorwerk, F. Sottile, and C. Draxl, Excitation pathways in resonant inelastic x-ray scattering of solids, *Phys. Rev. Res.* **2**, 042003 (2020).
- [26] D. Sangalli, M. d'Alessandro, and C. Attaccalite, Exciton-exciton transitions involving strongly bound excitons: An ab initio approach, *Physical Review B* **107**, 205203 (2023).
- [27] N. Farahani and D. Popova-Gorelova, Revealing fingerprints of valence excitons in x-ray absorption spectra with the bethe-salpeter equation, *Phys. Rev. B* **110**, 235126 (2024).
- [28] J. Ruan, Y.-H. Chan, and S. G. Louie, Exciton enhanced nonlinear optical responses in monolayer h-bn and mos2: Insight from first-principles exciton-state coupling formalism and calculations, *Nano Letters* **24**, 15533 (2024), pMID: 39556702.
- [29] C. Attaccalite and M. Grüning, Nonlinear optics from an ab initio approach by means of the dynamical berry phase: Application to second-and third-harmonic generation in semiconductors, *Physical Review B—Condensed Matter and Materials Physics* **88**, 235113 (2013).
- [30] I. Souza, J. Íñiguez, and D. Vanderbilt, Dynamics of berry-phase polarization in time-dependent electric fields, *Physical Review B* **69**, 085106 (2004).
- [31] R. King-Smith and D. Vanderbilt, Theory of polarization of crystalline solids, *Physical Review B* **47**, 1651 (1993).
- [32] R. Resta, Macroscopic polarization in crystalline dielectrics: the geometric phase approach, *Reviews of modern physics* **66**, 899 (1994).
- [33] M. N. Pionteck, M. Grüning, S. Sanna, and C. Attaccalite, A real-time approach to frequency-mixing spectroscopies: Application to sum and difference frequency generation in two-dimensional crystals, *SciPost Phys.* **19**,

- 129 (2025).
- [34] M. Grüning and C. Attacalite, Second harmonic generation in *h*-bn and mos₂ monolayers: Role of electron-hole interaction, *Phys. Rev. B* **89**, 081102 (2014).
- [35] C. Attacalite, E. Cannuccia, and M. Grüning, Excitonic effects in third-harmonic generation: The case of carbon nanotubes and nanoribbons, *Phys. Rev. B* **95**, 125403 (2017).
- [36] C. Attacalite, M. Grüning, H. Amara, S. Latil, and F. m. c. Ducastelle, Two-photon absorption in two-dimensional materials: The case of hexagonal boron nitride, *Phys. Rev. B* **98**, 165126 (2018).
- [37] M. N. Pionteck, M. Grüning, S. Sanna, and C. Attacalite, [Sum frequency generation from real-time simulations in two-dimensional crystals](#) (2025), [arXiv:2503.07095 \[cond-mat.mtrl-sci\]](#).
- [38] A. Marini, C. Hogan, M. Grüning, and D. Varsano, yambo: An ab initio tool for excited state calculations, *Computer Physics Communications* **180**, 1392 (2009).
- [39] D. Sangalli, A. Ferretti, H. Miranda, C. Attacalite, I. Marri, E. Cannuccia, P. Melo, M. Marsili, F. Paleari, A. Marrazzo, *et al.*, Many-body perturbation theory calculations using the yambo code, *Journal of Physics: Condensed Matter* **31**, 325902 (2019).
- [40] A. Gulans, S. Kontur, C. Meisenbichler, D. Nabok, P. Pavone, S. Rigamonti, S. Sagmeister, U. Werner, and C. Draxl, Exciting: a full-potential all-electron package implementing density-functional theory and many-body perturbation theory, *Journal of Physics: Condensed Matter* **26**, 363202 (2014).
- [41] R. R. Pela and C. Draxl, All-electron full-potential implementation of real-time tddft in exciting, *Electronic Structure* **3**, 037001 (2021).
- [42] M. Raya-Moreno, N. A. Dasch, N. Farahani, I. G. Oliva, A. Gulans, M. Hossain, H. Kleine, M. Kuban, S. Lubeck, B. Maurer, P. Pavone, F. Peschel, D. Popova-Gorelova, L. Qiao, E. Richter, S. Rigamonti, R. R. Pela, K. Sinha, D. T. Speckhard, S. Tillack, D. Tumakov, S. Hong, J. Użulis, M. Voiculescu, C. Vona, M. Yang, and C. Draxl, [An exciting approach to theoretical spectroscopy](#) (2026), [arXiv:2601.11388 \[cond-mat.mtrl-sci\]](#).
- [43] Z. Liu, L. Ma, G. Shi, W. Zhou, Y. Gong, S. Lei, X. Yang, J. Zhang, J. Yu, K. P. Hackenberg, *et al.*, In-plane heterostructures of graphene and hexagonal boron nitride with controlled domain sizes, *Nature nanotechnology* **8**, 119 (2013).
- [44] K. Ba, W. Jiang, J. Cheng, J. Bao, N. Xuan, Y. Sun, B. Liu, A. Xie, S. Wu, and Z. Sun, Chemical and bandgap engineering in monolayer hexagonal boron nitride, *Scientific reports* **7**, 45584 (2017).
- [45] C. Elias, P. Valvin, T. Pelini, A. Summerfield, C. Mellor, T. Cheng, L. Eaves, C. Foxon, P. Beton, S. Novikov, *et al.*, Direct band-gap crossover in epitaxial monolayer boron nitride, *Nature communications* **10**, 2639 (2019).
- [46] R. J. P. Román, F. J. C. Costa, A. Zobelli, C. Elias, P. Valvin, G. Cassabo, B. Gil, A. Summerfield, T. S. Cheng, C. J. Mellor, *et al.*, Band gap measurements of monolayer h-bn and insights into carbon-related point defects, *2D Materials* **8**, 044001 (2021).
- [47] G. Cassabo, P. Valvin, and B. Gil, Hexagonal boron nitride is an indirect bandgap semiconductor, *Nature photonics* **10**, 262 (2016).
- [48] T. Galvani, F. Paleari, H. P. C. Miranda, A. Molina-Sánchez, L. Wirtz, S. Latil, H. Amara, and F. m. c. Ducastelle, Excitons in boron nitride single layer, *Phys. Rev. B* **94**, 125303 (2016).
- [49] R. Roldán, L. Chirolli, E. Prada, J. A. Silva-Guillén, P. San-Jose, and F. Guinea, Theory of 2d crystals: graphene and beyond, *Chemical Society Reviews* **46**, 4387 (2017).
- [50] D. Wickramaratne, L. Weston, and C. G. Van de Walle, Monolayer to bulk properties of hexagonal boron nitride, *The Journal of Physical Chemistry C* **122**, 25524 (2018).
- [51] F. Ferreira, A. Chaves, N. Peres, and R. Ribeiro, Excitons in hexagonal boron nitride single-layer: a new platform for polaritonics in the ultraviolet, *Journal of the Optical Society of America B* **36**, 674 (2019).
- [52] S. Roy, X. Zhang, A. B. Puthirath, A. Meiyazhagan, S. Bhattacharyya, M. M. Rahman, G. Babu, S. Susarla, S. K. Saju, M. K. Tran, L. M. Sassi, M. A. S. R. Saadi, J. Lai, O. Sahin, S. M. Sajadi, B. Dharmarajan, D. Salpekar, N. Chakingal, A. Baburaj, X. Shuai, A. Adumbumkulath, K. A. Miller, J. M. Gayle, A. Ajnsztajn, T. Prasankumar, V. V. J. Harikrishnan, V. Ojha, H. Kannan, A. Z. Khater, Z. Zhu, S. A. Iyengar, P. A. d. S. Autreto, E. F. Oliveira, G. Gao, A. G. Birdwell, M. R. Neupane, T. G. Ivanov, J. Taha-Tijerina, R. M. Yadav, S. Arepalli, R. Vajtai, and P. M. Ajayan, Structure, properties and applications of two-dimensional hexagonal boron nitride, *Advanced Materials* **33**, 2101589 (2021).
- [53] A. Rousseau, L. Ren, A. Durand, P. Valvin, B. Gil, K. Watanabe, T. Taniguchi, B. Urbaszek, X. Marie, C. Robert, *et al.*, Monolayer boron nitride: Hyperspectral imaging in the deep ultraviolet, *Nano Letters* **21**, 10133 (2021).
- [54] A. Kirchoff, T. Deilmann, P. Krüger, and M. Rohlfing, Electronic and optical properties of a hexagonal boron nitride monolayer in its pristine form and with point defects from first principles, *Phys. Rev. B* **106**, 045118 (2022).
- [55] F. Zhang, C. S. Ong, J. W. Ruan, M. Wu, X. Q. Shi, Z. K. Tang, and S. G. Louie, Intervalley excitonic hybridization, optical selection rules, and imperfect circular dichroism in monolayer *h*-BN, *Phys. Rev. Lett.* **128**, 047402 (2022).
- [56] F. Li, X. Liu, Y. Wang, and Y. Li, Germanium monosulfide monolayer: a novel two-dimensional semiconductor with a high carrier mobility, *Journal of Materials Chemistry C* **4**, 2155 (2016).
- [57] V. Khuong Dien, P. Thi Bich Thao, N. Thi Han, N. Duy Khanh, L. V. Phuong Thuan, M.-F. Lin, and N. Thanh Tien, Strain-controlled electronic transport and exciton radiative lifetime in monolayer germanium sulfide, *Phys. Rev. B* **108**, 205406 (2023).
- [58] J. Esteve-Paredes, M. García-Blázquez, A. Uría-Álvarez, M. Camarasa-Gómez, and J. Palacios, Excitons in non-linear optical responses: shift current in mos₂ and ges monolayers, *npj Computational Materials* **11**, 13 (2025).
- [59] D. A. Wheeler and J. Z. Zhang, Exciton dynamics in semiconductor nanocrystals, *Advanced Materials* **25**, 2878 (2013).
- [60] S. L. Adler, Quantum theory of the dielectric constant in real solids, *Phys. Rev.* **126**, 413 (1962).
- [61] G. A. Baraff and M. Schlüter, Migration of interstitials in silicon, *Phys. Rev. B* **30**, 3460 (1984).
- [62] G. Onida, L. Reining, and A. Rubio, Electronic excitations: density-functional versus many-body green's-function approaches, *Rev. Mod. Phys.* **74**, 601 (2002).

- [63] L. Hedin, New method for calculating the one-particle green's function with application to the electron-gas problem, *Phys. Rev.* **139**, A796 (1965).
- [64] M. S. Hybertsen and S. G. Louie, Electron correlation in semiconductors and insulators: Band gaps and quasiparticle energies, *Physical Review B* **34**, 5390 (1986).
- [65] G. Strinati, Application of the green's functions method to the study of the optical properties of semiconductors, *La Rivista del Nuovo Cimento (1978-1999)* **11**, 1 (1988).
- [66] D. Sangalli, J. A. Berger, C. Attaccalite, M. Grüning, and P. Romaniello, Optical properties of periodic systems within the current-current response framework: Pitfalls and remedies, *Phys. Rev. B* **95**, 155203 (2017).
- [67] M. Springborg and B. Kirtman, Analysis of vector potential approach for calculating linear and nonlinear responses of infinite periodic systems to a finite static external electric field, *Phys. Rev. B* **77**, 045102 (2008).
- [68] I. Souza, J. Íñiguez, and D. Vanderbilt, First-principles approach to insulators in finite electric fields, *Physical review letters* **89**, 117602 (2002).
- [69] D. Snoke, Predicting the ionization threshold for carriers in excited semiconductors, *Solid State Communications* **146**, 73 (2008).
- [70] E. Perfetto, A. Marini, and G. Stefanucci, Self-consistent screening enhances the stability of the nonequilibrium excitonic insulator phase, *Phys. Rev. B* **102**, 085203 (2020).
- [71] R. W. Nunes and X. Gonze, Berry-phase treatment of the homogeneous electric field perturbation in insulators, *Phys. Rev. B* **63**, 155107 (2001).
- [72] C. Vorwerk, B. Aurich, C. Cocchi, and C. Draxl, Bethe-salpeter equation for absorption and scattering spectroscopy: implementation in the exciting code, *Electronic Structure* **1**, 037001 (2019).
- [73] J. P. Perdew, A. Ruzsinszky, G. I. Csonka, O. A. Vydrov, G. E. Scuseria, L. A. Constantin, X. Zhou, and K. Burke, Restoring the density-gradient expansion for exchange in solids and surfaces, *Phys. Rev. Lett.* **100**, 136406 (2008).
- [74] F. Paleari, T. Galvani, H. Amara, F. Ducastelle, A. Molina-Sánchez, and L. Wirtz, Excitons in few-layer hexagonal boron nitride: Davydov splitting and surface localization, *2D Materials* **5**, 045017 (2018).
- [75] M. S. Dresselhaus, G. Dresselhaus, and A. Jorio, *Group theory: application to the physics of condensed matter* (Springer Science & Business Media, 2007).